# Surface wrinkling of a channelized flow

By A. C. Slim[1], N. J. Balmforth[1,2], R. V. Craster[3] and J. C. Miller[4]

[1] Department of Mathematics, University of British Columbia, 1984 Mathematics Road, Vancouver, BC, V6T 1Z2, Canada

[2] Department of Earth and Ocean Sciences, University of British Columbia, 6339 Stores Road, Vancouver, BC, V6T 1Z4, Canada

[3] Department of Mathematics, Imperial College London, South Kensington Campus, London, SW7 2AZ, U.K.

[4] Division of Mathematical Modeling, University of British Columbia Centre for Disease Control, 655 West 12th Avenue, Vancouver, BC, V5Z 4R4, Canada

We consider an inclined rectangular duct of constant cross-section conveying Newtonian fluid and covered by a thin, Hookean isotropic elastic solid. The elastic plate is described by the Föppl–von Kármán equations, and the fluid by the Stokes equations. The equations admit an equilibrium solution in which the plate is flat and fluid flows underneath due to gravity. This base flow induces a varying traction across the elastic plate, which opens up the possibility of out-of-plane buckling due to the associated in-plane shear. A linear stability analysis demonstrates that buckling occurs for sufficiently thin plates on steep slopes and deep channels. The most unstable modes take the form of either symmetric or antisymmetric downslope-directed chevrons that travel downstream at a fraction of the average speed of the base flow. An analogous analysis shows that similar buckling also occurs if the elastic plate is replaced by a thin skin of very viscous fluid. Our description provides a simple model for the formation of ropy pahoehoe lava.

**Keywords: Elastic plate; buckling; lava flow; ropy pahoehoe**

## 1. Introduction

The interaction of a fluid with an overlying elastic "skin" (or, indeed, any rheologically distinct and thin superficial layer), can generate a variety of buckling patterns. Common examples include the wrinkling of the thin skins that form atop hot milk, wax or crème anglais when disturbed. Likewise, it has been suggested that motion of the molten interior of a lava flow can buckle the overlying solidified crust, creating a characteristic "ropy" appearance (Fink & Fletcher, 1978); see figure 1. In these examples, the fluid flow plays an essential role in promoting the buckling of the skin, for example, by advecting it towards a boundary and thus compressing it. However, the fluid can also play a more passive role, such as in semiconductor manufacturing where an elastic plate floating on a viscous layer is compressed by external forces with the fluid acting merely to control the timescale of buckling (Huang & Suo, 2002).

Our goal is to explore a model problem in which fluid flow directly induces buckling. We consider the gravity-driven flow of a viscous fluid through a rectangular duct overlain by a thin elastic plate. Because the flow is driven by gravity alone,

Figure 1. A solidified lava flow at Kealakomo, Hawaii courtesy of Dr. Ron Schott.

without a pressure gradient, an equilibrium state can be established in which the surface skin remains flat. This equilibrium and its linear perturbations can be described with relative mathematical simplicity, in contrast to pressure-driven flows which necessarily differentially deform the overlying skin in the downstream direction. The fluid traction acting on the base of the skin varies across the duct and thus generates shear within it, potentially inducing out-of-plane buckling when tractions are sufficient strong. This configuration is one of the simplest idealizations of the particular fluid-structure interaction problem in question, and bears similarities with the buckling of an isolated elastic plate either under gravity or shear (Balmforth *et al.*, 2008).

More technically, we treat the viscous fluid with the Stokes approximation, restricting our attention to relatively slow viscous flows. We model the elastic plate as a thin, Hookean isotropic elastic solid satisfying the Föppl–von Kármán equations (Love, 1944). These are the simplest plate equations that incorporate both the bending and compressional terms necessary to account for out-of-plane buckling. The choice of this model for the skin is not essential, and we supplement our study of the elastically-plated duct with an exploration of a related problem in which the skin is composed of a yet-more-viscous, thin immiscible fluid.

Despite the common occurrence of fluid-induced buckling of a superficial skin, relatively few preceding studies exist on the problem. Perhaps the closest earlier work to our current study is by Luo & Pozrikidis (2006, 2007). They considered the buckling of an arbitrarily-shaped elastic section in an otherwise rigid plate suspended in flowing fluid. Both a compressive stress against the upstream rigid boundary and a shear stress are induced in the elastic section by the flow, resulting in a complicated buckling instability. However, although the elastic portion of the plate deforms out of its plane on buckling, these authors do not incorporate the resulting feedback on the fluid dynamics with the result that there are no induced pressure variations on either side of the plate. This simplifies the analysis, but alters the nature of the instability since fluid pressure cannot provide a restoring force.

The paper is structured as follows. In §2 we formulate the problem and note the assumptions required. In §3 we present the flat base state profile that we perturb about. We analyze the linear stability numerically in §4. A brief comparison of this theory with a qualitative experiment is presented in §5. In §6, we consider the
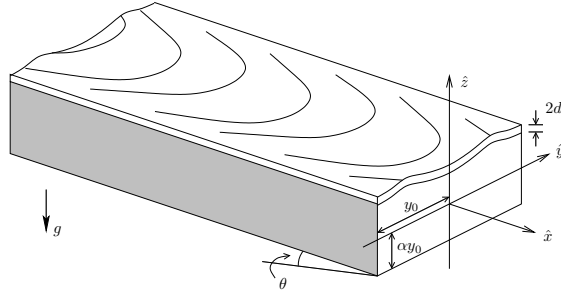
Figure 2. An inclined rectangular duct with rigid base and sides and a thin elastic plate as the top surface. Fluid supplied far upslope fills the channel and flows downslope under the influence of gravity alone.

particular geological application of ropy pahoehoe lava. Finally in §7 we present our most significant findings. Appendix A furnishes the derivation of the Föppl–von Kármán equations in the present context and outlines their limits of validity. Appendix B briefly discusses the supplementary problem in which the elastic skin is replaced by a very viscous fluid one.

## 2. Formulation

As illustrated in figure 2, we consider a duct of infinite length and rectangular cross-section (having width $2y_0$ and depth $2\alpha y_0$, where $\alpha$ is the aspect ratio) inclined at angle $\theta$ to the horizontal. The duct is described by a Cartesian coordinate system with $\hat{x}$ directed downslope, $\hat{y}$ across the slope and $\hat{z}$ perpendicular to the slope; the origin is located on the centre-line. The bottom, $\hat{z} = -\alpha y_0$, and sides, $\hat{y} = \pm y_0$, are rigid; the top, $\hat{z} = \alpha y_0 + \hat{\zeta}(\hat{x}, \hat{y}, \hat{t})$, is an isotropic Hookean elastic plate of thickness $2d \ll 2y_0$, Young's modulus $E$ and Poisson ratio $\nu$, where $\hat{\zeta}$ is the out-of-plane displacement of the preferentially flat plate. An incompressible, inertialess Newtonian fluid of density $\rho$ and viscosity $\mu$ fills the duct and flows downslope under gravity.

The fluid motion is described by Stokes' equations

$$\hat{\nabla} \cdot \hat{\boldsymbol{\sigma}} = \rho g(-\sin\theta, 0, \cos\theta), \quad \hat{\boldsymbol{\sigma}} = -\hat{p}\mathsf{I} + \mu\left(\hat{\boldsymbol{\nabla}}\hat{\mathbf{u}} + \hat{\boldsymbol{\nabla}}\hat{\mathbf{u}}^\dagger\right), \quad \hat{\nabla} \cdot \hat{\mathbf{u}} = 0, \quad (2.1)$$

where $\hat{\boldsymbol{\nabla}} = (\partial/\partial\hat{x}, \partial/\partial\hat{y}, \partial/\partial\hat{z})$, $\hat{\boldsymbol{\sigma}}$ is the stress tensor, $g$ the acceleration due to gravity, $\hat{p}$ the pressure, $\hat{\mathbf{u}}$ the velocity, $\mathsf{I}$ the identity tensor and $\dagger$ denotes the transpose. On the rigid lower and side surfaces of the duct we impose no-slip

$$\hat{\mathbf{u}} = \mathbf{0} \quad \text{on } \hat{y} = \pm y_0, \ \hat{z} = -\alpha y_0. \quad (2.2)$$

The displacement gradients in the elastic plate are assumed to be small so that it may be described by the Föppl–von Kármán equations in Eulerian coordinates. In Appendix A we give a discussion of the underlying assumptions that are required for these equations to apply. We also assume that the weight of the plate is negligible compared to fluid tractions acting upon it and that elastic waves are much faster than the adjustment time scale of the coupled elastic-fluid system so that the plate

can be assumed in instantaneous equilibrium. Thus the in-plane and out-of-plane force balances are given by

$$\hat{\nabla}_h \cdot \hat{\mathsf{N}} = \hat{\boldsymbol{\tau}}_h, \quad \frac{2d^3 E}{3(1-\nu^2)} \hat{\nabla}_h^4 \hat{\zeta} = -\hat{\tau}_z + \hat{\nabla}_h \cdot \left( \hat{\mathsf{N}} \cdot \hat{\boldsymbol{\nabla}}_h \hat{\zeta} \right), \quad (2.3)$$

respectively, where the subscript $h$ denotes in-plane ($\hat{x}$ and $\hat{y}$) components, $\hat{\nabla}_h^4 = (\partial^2/\partial \hat{x}^2 + \partial^2/\partial \hat{y}^2)^2$ and $\hat{\boldsymbol{\tau}} = (\hat{\boldsymbol{\tau}}_h, \hat{\tau}_z)$ is the fluid traction acting on the base of the plate. Here the in-plane stresses (integrated over the thickness) and strains are

$$\hat{\mathsf{N}} = \frac{2dE}{1-\nu^2} \left[ \nu \operatorname{tr}(\hat{\mathsf{e}}) \mathsf{I}_h + (1-\nu)\hat{\mathsf{e}} \right], \quad \hat{\mathsf{e}} = \frac{1}{2} \left( \hat{\boldsymbol{\nabla}}_h \hat{\boldsymbol{\xi}} + \hat{\boldsymbol{\nabla}}_h \hat{\boldsymbol{\xi}}^\dagger + \hat{\boldsymbol{\nabla}}_h \hat{\zeta} \hat{\boldsymbol{\nabla}}_h \hat{\zeta} \right), \quad (2.4)$$

respectively, where $\hat{\boldsymbol{\xi}} = (\hat{\xi}, \hat{\eta})$ is the in-plane displacement and $\operatorname{tr}(\cdot)$ is the trace. The plate is clamped along its lateral edges

$$\hat{\xi} = \hat{\eta} = \hat{\zeta} = \frac{\partial \hat{\zeta}}{\partial \hat{y}} = 0 \quad \text{on } \hat{y} = \pm y_0. \quad (2.5)$$

The plate displacement and fluid velocities are connected through the kinematic boundary condition

$$\hat{u} = \hat{v} = 0, \ \hat{w} = \frac{\partial \hat{\zeta}}{\partial \hat{t}} \quad \text{on } \hat{z} = \alpha y_0 + \hat{\zeta}, \quad (2.6)$$

where $\hat{t}$ is time and we have neglected the $\hat{\mathbf{u}} \cdot \hat{\boldsymbol{\nabla}}(\hat{\xi}, \hat{\eta}, \hat{\zeta})$ and time-derivative terms in the in-plane equations for consistency with the required scalings for the Föppl–von Kármán equations. The traction on the plate $\hat{\boldsymbol{\tau}}$ is exerted by fluid shear stresses

$$\hat{\boldsymbol{\tau}} = \hat{\boldsymbol{\sigma}} \cdot \hat{\mathbf{n}} \quad \text{on } \hat{z} = \alpha y_0 + \hat{\zeta}, \quad (2.7)$$

where $\hat{\mathbf{n}}$ is the normal to the plate.

### (a) Non-dimensionalization

We non-dimensionalize the governing equations based on the half-width of the channel and the gravitational driving force as follows:

$$\hat{\mathbf{u}} = \mathbf{u}\, \rho g y_0^2 / \mu, \quad \hat{p} = p\, \rho g y_0, \quad \hat{\boldsymbol{\sigma}} = \boldsymbol{\sigma} \rho g y_0, \quad \hat{\boldsymbol{\tau}} = \boldsymbol{\tau} \rho g y_0,$$
$$\hat{\boldsymbol{\xi}} = \boldsymbol{\xi}\, y_0, \quad \hat{\zeta} = \zeta\, y_0, \quad \hat{\mathsf{N}} = \mathsf{N}\, \rho g y_0^2, \quad \hat{\mathsf{e}} = \mathsf{e}, \quad \hat{\mathbf{x}} = \mathbf{x}\, y_0, \quad \hat{t} = t\, \mu / \rho g y_0. \quad (2.8)$$

Substituting (2.8) into (2.1)–(2.7) we obtain

$$\nabla \cdot \boldsymbol{\sigma} = (-\sin\theta, 0, \cos\theta), \quad \boldsymbol{\sigma} = -p\mathsf{I} + \boldsymbol{\nabla}\mathbf{u} + \boldsymbol{\nabla}\mathbf{u}^\dagger, \quad \nabla \cdot \mathbf{u} = 0, \quad (2.9)$$

subject to

$$\mathbf{u} = \mathbf{0} \quad \text{on } y = \pm 1, \ z = -\alpha, \quad (2.10)$$

$$u = v = 0, \ w = \frac{\partial \zeta}{\partial t} \quad \text{on } z = \alpha + \zeta. \quad (2.11)$$

This flow field is coupled to the plate through

$$\nabla_h \cdot \mathsf{N} = \boldsymbol{\tau}_h, \quad \frac{1}{\mathcal{G}} \nabla_h^4 \zeta = -\tau_z + \nabla_h \cdot (\mathsf{N} \cdot \boldsymbol{\nabla}_h \zeta), \tag{2.12}$$

with

$$G\mathsf{N} = \nu \, \mathrm{tr}(\mathsf{e}) \mathsf{I}_h + (1-\nu)\mathsf{e}, \;\; \mathsf{e} = \frac{1}{2}\left(\boldsymbol{\nabla}\boldsymbol{\xi} + \boldsymbol{\nabla}\boldsymbol{\xi}^\dagger + \boldsymbol{\nabla}\zeta\boldsymbol{\nabla}\zeta\right), \;\; \boldsymbol{\tau} = \boldsymbol{\sigma}|_{z=\alpha+\zeta} \cdot \mathbf{n}, \tag{2.13}$$

subject to

$$\xi = \eta = \zeta = \frac{\partial \zeta}{\partial y} = 0 \quad \text{on } y = \pm 1. \tag{2.14}$$

The dimensionless parameters remaining are the inclination of the duct $\theta$, aspect ratio of the duct $\alpha$, Poisson ratio of the plate $\nu$,

$$\mathcal{G} = \frac{3(1-\nu^2)\rho g y_0^4}{2d^3 E} \tag{2.15}$$

measuring the relative importance of fluid forcing to bending stiffness and $G = \mathcal{G}d^2/3y_0^2$. Only $\mathcal{G}$, $\theta$ and $\alpha$ appear in the linear stability analysis.

## 3. Base state

Our base state (denoted by subscript 0) is driven by gravity alone; the plate is flat and the flow is steady and unidirectional. The flow profile is decoupled from the in-plane distortion of the plate and is precisely that for a rigid rectangular duct (Rosenhead, 1963):

$$\frac{2}{\sin\theta} u_0(y,z) = \alpha^2 - z^2 - 4\alpha^2 \left(\frac{2}{\pi}\right)^3 \sum_{n=0}^\infty \frac{(-1)^n}{(2n+1)^3} \frac{\cosh\frac{(2n+1)\pi y}{2\alpha}}{\cosh\frac{(2n+1)\pi}{2\alpha}} \cos\frac{(2n+1)\pi z}{2\alpha}, \tag{3.1}$$

with $v_0 = w_0 = 0$ and $p_0 = (\alpha - z)\cos\theta$.

The fluid flow imposes a traction on the base of the plate, causing downstream stretching according to

$$\frac{(1-\nu)}{G\sin\theta} \xi_0(y) = \alpha(1-y^2) - \frac{2}{3}\alpha^3 + \left(\frac{2}{\pi}\right)^4 \sum_{n=0}^\infty \frac{4\alpha^3}{(2n+1)^4} \frac{\cosh\frac{(2n+1)\pi y}{2\alpha}}{\cosh\frac{(2n+1)\pi}{2\alpha}}, \tag{3.2}$$

with $\eta_0 = \zeta_0 = 0$. For convenience we define a scaled shear stress in the plate as

$$\mathcal{S}(y,\alpha) = \frac{(1-\nu)}{G\sin\theta}\frac{\partial\xi_0}{\partial y} = -2\alpha y + \left(\frac{2}{\pi}\right)^3 \sum_{n=0}^\infty \frac{4\alpha^2}{(2n+1)^3} \frac{\sinh\frac{(2n+1)\pi y}{2\alpha}}{\cosh\frac{(2n+1)\pi}{2\alpha}}. \tag{3.3}$$

Sample base state velocity profiles and displacements are shown in figure 3.

## 4. Linear stability

To examine the stability of the base state, we perturb each of the variables about it, $f = f_0 + f_1$, where $f$ denotes any of $u$, $v$, $w$, $p$ and $\zeta$, and the subscript 1 refers to
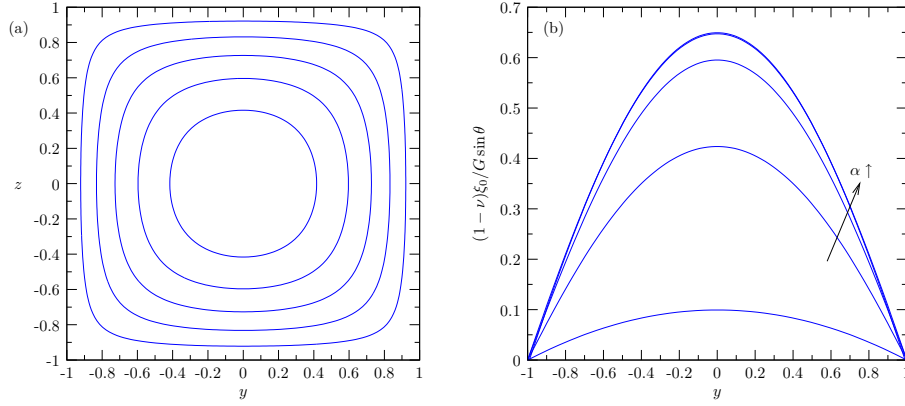
Figure 3. The base state (a) downslope velocity profile $2u_0/\sin\theta$ for $\alpha = 1$ (contours at intervals of 0.1 from 0.1) and (b) downslope plate displacement profile $(1-\nu)\xi_0/G\sin\theta$ for $\alpha = 0.1, 0.5, 1, 2$ and $10$.

the perturbation. We then linearize in the perturbation amplitudes $f_1$ and calculate the growth rate, $\omega = \omega_r + i\omega_i$, of infinitesimal normal mode perturbations with downstream wavenumber $k$: $f_1 = \hat{f}_1(y,z)e^{ikx-i\omega t}$. This furnishes the eigenvalue problem:

$$-k^2 u_1 + \frac{\partial^2 u_1}{\partial y^2} + \frac{\partial^2 u_1}{\partial z^2} = ikp_1, \tag{4.1}$$

$$-k^2 v_1 + \frac{\partial^2 v_1}{\partial y^2} + \frac{\partial^2 v_1}{\partial z^2} = \frac{\partial p_1}{\partial y}, \tag{4.2}$$

$$-k^2 w_1 + \frac{\partial^2 w_1}{\partial y^2} + \frac{\partial^2 w_1}{\partial z^2} = \frac{\partial p_1}{\partial z}, \tag{4.3}$$

$$iku_1 + \frac{\partial v_1}{\partial y} + \frac{\partial w_1}{\partial z} = 0, \tag{4.4}$$

with boundary conditions

$$u_1 = v_1 = w_1 = 0 \text{ on } y = \pm 1, \ z = -\alpha, \tag{4.5}$$

$$u_1 + \frac{1}{2}\frac{\partial \mathcal{S}}{\partial y}\zeta_1 \sin\theta = v_1 = w_1 + i\omega\zeta_1 = 0 \text{ on } z = \alpha, \tag{4.6}$$

where

$$\frac{1}{\mathcal{G}}\left(\frac{\partial^4 \zeta_1}{\partial y^4} - 2k^2\frac{\partial^2 \zeta_1}{\partial y^2} + k^4\zeta_1\right) = p_1 - \zeta_1 \cos\theta + ik\mathcal{S}\frac{\partial \zeta_1}{\partial y}\sin\theta, \tag{4.7}$$

and

$$\zeta_1 = \frac{\partial \zeta_1}{\partial y} = 0 \quad \text{on } y = \pm 1. \tag{4.8}$$

Here the in-plane displacement equations are omitted because they decouple from the remainder of the linearized system.

We solved the system (4.1)–(4.8) numerically using a Chebyshev collocation scheme (Trefethen, 2000) with the boundary conditions imposed explicitly (Weideman & Reddy, 2000) and $u_1$ and $p_1$ eliminated. The resulting generalized eigenvalue
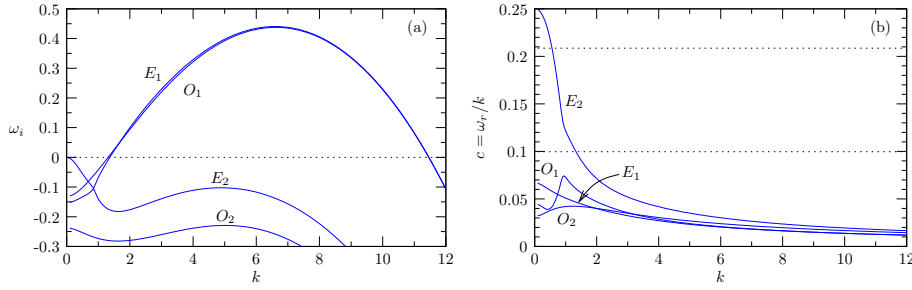
Figure 4. (a) Growth rate and (b) wavespeed for the four least stable modes with $\alpha = \tan\theta = 1$ and $\mathcal{G} = 1000$. Here $E$ denotes an even mode and $O$ an odd mode. The dotted lines in (b) indicate the centre-line velocity and the average velocity of the base flow.

problem was solved using the QZ-algorithm. We found that employing an equal number of collocation points in each direction yielded reasonably fast convergence rates for most values of $\alpha$ (presumably because the boundary layers in both $y$ and $z$ are important). The method required prohibitively many points for large $k$ resulting in some incomplete curves in the data shown in figures 5 and 7.

The dispersion relations for the four least-stable modes with $\alpha = \tan\theta = 1$ and $\mathcal{G} = 1000$ are plotted in figure 4. For $k \to 0$, the dominant mode $E_2$ corresponds to uniformly over- or underfilling the channel and travels faster than the base-state flow. At intermediate and large wavenumbers, an even $E_1$ and odd $O_1$ pair of modes dominate, and for a range of intermediate wavenumbers are unstable. These modes are destabilized by the traction exerted by the fluid on the base of the plate. They are stabilized at large wavenumber by bending stiffness and at small wavenumber by a combination of bending stiffness and the restoring pressure force of the fluid. The odd mode is more unstable at small $k$, but the even mode becomes dominant at intermediate $k$. This competition reflects the delicate balance between cross-slope and downslope bending; the former favours the odd mode while the latter favours the even mode. At large wavenumber, the eigenfunctions become concentrated near the sidewalls where there is maximum shear and there is little deflection near the centre-line, with the result that the modal growth rates become indistinguishable. The unstable waves propagate downslope at a fraction of the average base state velocity. A multitude of other modes exist with decreasing growth rate, as illustrated by the additional odd mode $O_2$ in figure 4.

The growth rates and phase speed of the most unstable mode are shown on the $(k, \mathcal{G})$-plane for $\alpha = \tan\theta = 1$ in figure 5. The flat base state becomes unstable above a critical value, $\mathcal{G} = \mathcal{G}_c$, over an increasingly wide window of wavenumbers. The most unstable modes are found at increasingly shorter wavelengths and have slowly decreasing wavespeeds. A selection of neutral stability curves for different slope angles and aspect ratios is shown in figure 6. For steeper slopes, onset occurs for smaller driving forces and for longer waves because the component of gravity driving the underlying shear flow is increased and the stabilizing hydrostatic pressure reduced. As the channel becomes deeper, onset occurs at smaller driving force and longer waves because larger shear stresses can be generated on the plate. How-
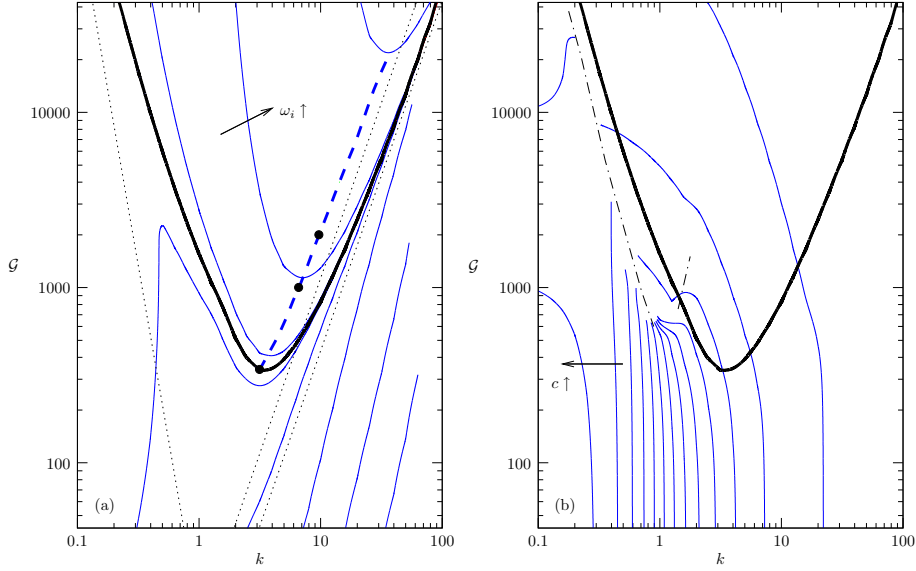
Figure 5. Dispersion relation for the least stable mode in $(k, \mathcal{G})$ for $\alpha = \tan \theta = 1$. (a) Properties of the growth rate: thin solid curves are contours of $\omega_i$ drawn at $-500$, $-50$, $-5$, $-0.5$, $-0.05$, $0.05$, $0.5$ and $5$; the bold curve indicates neutral stability. The dashed bold curve locates the least stable wavenumber for given $\mathcal{G}$. Dotted lines are local analysis approximations for the long- and short-wave cut-offs and least-stable wavenumber. (b) Properties of the wave speed: thin curves are contours of $c = \omega_r/k$ drawn at intervals of $0.02$ from $0.01$. The dash-dotted curves give the approximate locations of a change in the dominant mode, where the wavespeed is discontinuous (this jump is not indicated where it is relatively small).
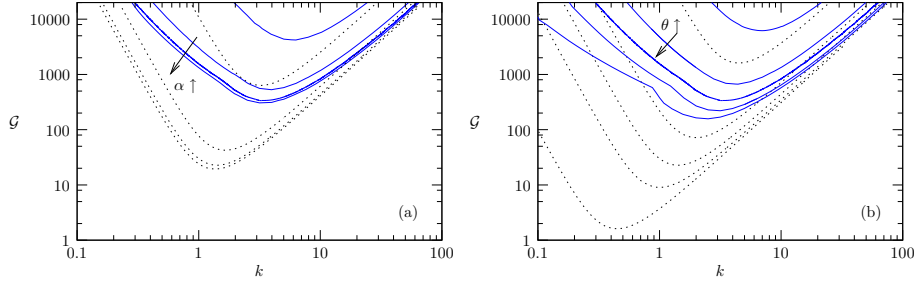


Figure 6. Neutral stability curves (solid) for (a) $\tan \theta = 1$ and $\alpha = 0.1$, $0.5$, $1$ and $2$; (b) $\alpha = 1$ and $\tan \theta = 0.1$, $0.5$, $1$, $2$ and $10$. Dotted curves are the corresponding local analysis approximations.

ever, the behaviour becomes independent of the aspect ratio once $\alpha$ exceeds two or so.

The behaviour of the critical value $\mathcal{G}_c$ as a function of slope angle and aspect ratio is illustrated in figure 7. Panel (a) also displays contours of growth rate, phase speed and wavenumber for the most unstable mode above onset with $\alpha = 1$.
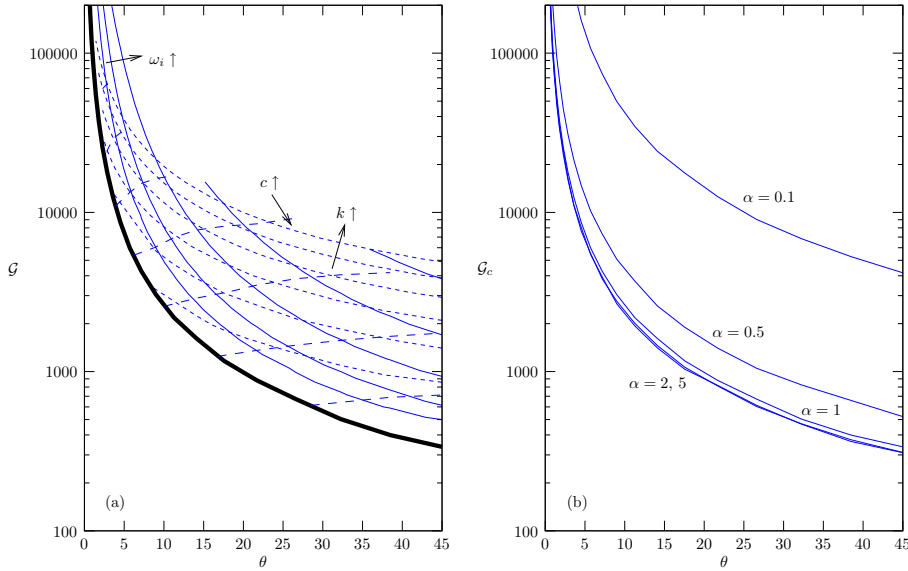
Figure 7. (a) Properties of the least stable mode in $(\theta, \mathcal{G})$-space for $\alpha = 1$. Solid curves are contours of growth rate, drawn at $0.1 \times 2^j$, $j = 0,\ldots,4$; the bold curve is the neutral stability curve below which the pressure mode with $k = 0$ dominates. Long-dashed curves are contours of wavespeed, drawn at $0.0001 \times 2^j$, $j = 2,\ldots,8$. Short-dashed curves are contours of wavenumber, drawn at intervals of 2 from $k = 6$. Insufficient numerical accuracy prevented further details for large $\theta$ and $\mathcal{G}$. (b) Neutral stability curves in $(\theta, \mathcal{G})$ space for $\alpha = 0.1$, 0.5, 1, 2 and 5.

Finally, figures 8 and 9 present mode profiles for the two most unstable modes (here $E_1$ and $O_1$) at the $\mathcal{G}$-values marked in figure 5 ($\alpha = \tan\theta = 1$). The out-of-plane displacement takes the form of downslope-directed chevrons with the crests having an appreciable angle to the axis of the channel, despite the base displacement being small [*c.f.* the shear-induced buckles of an isolated elastic plate (Mansfield, 1964; Wong & Pellegrino, 2006; Balmforth *et al.*, 2008)]. The figure also highlights the increasing concentration of the eigenfunctions to the regions near the sidewalls with increasing $\mathcal{G}$ and $k$. At onset, the perturbation to the velocity field is appreciable throughout the depth of the channel but with larger growth rates only the uppermost fluid layer responds to the plate motion.

### (*a*) *Local analysis*

A crude short-wavelength-style analysis in which we assume that perturbations vary rapidly in $y$ compared to the variation of the background state provides analytical estimates to complement the numerical stability theory. Decomposing the perturbations as $f_1 = \check{f}_1(z)e^{ikx+imy-i\omega t}$, we integrate the fluid equations through the depth of the flow and impose the boundary conditions at $z = \pm\alpha$ to obtain a "dispersion relation",

$$\omega = \frac{-k\sinh^2(2\alpha\kappa)\frac{\partial\mathcal{S}}{\partial y}\sin\theta + i[4\alpha^2\kappa^2 - \sinh^2(2\alpha\kappa)]\chi}{4\alpha\kappa + \sinh(4\alpha\kappa)}, \tag{4.9}$$
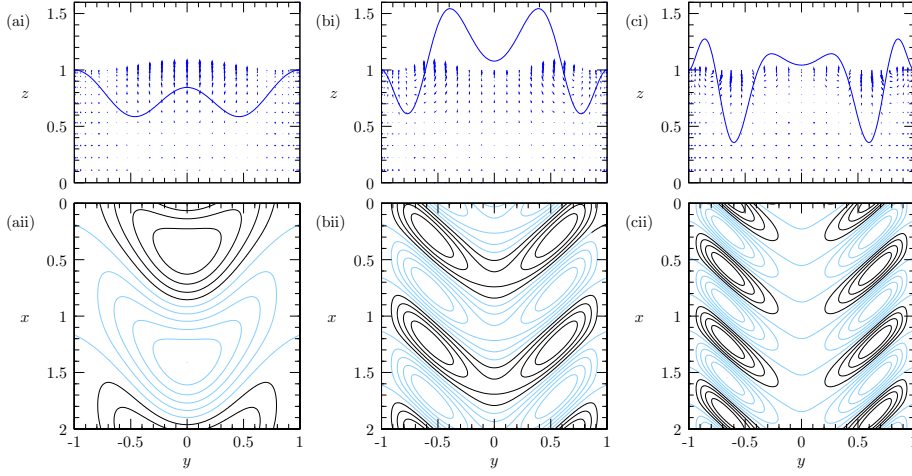
Figure 8. Lower panels: out-of-plane displacement profiles with contours at intervals of 0.2 of the maximum. Lighter (darker) curves indicate positive (negative) displacements. Upper panels: cross-slope velocity profiles $(v, w)$ in the upper half of the channel and out-of-plane displacements at $x = 0$ in the corresponding lower panel. Plots are for the most unstable mode $E_1$ at (a) approximate onset, $\mathcal{G} = 337$, (b) $\mathcal{G} = 1000$ and (c) $\mathcal{G} = 2000$ with $\alpha = \tan\theta = 1$ and correspond to the discs in figure 5.
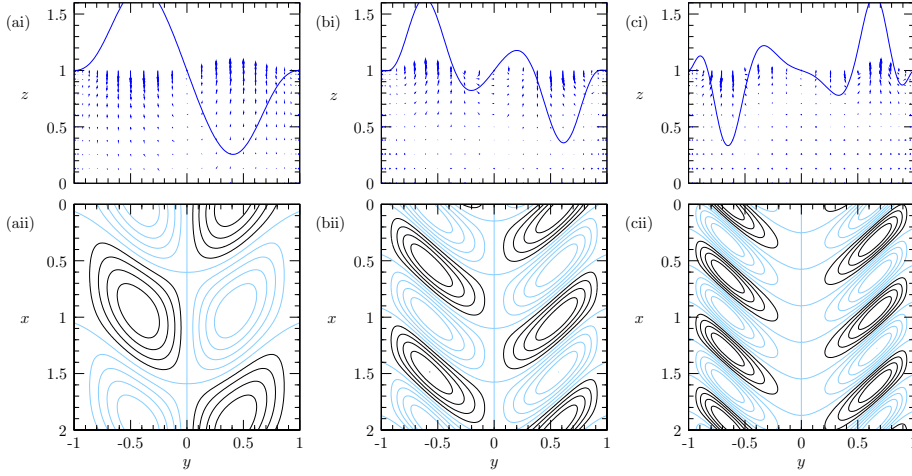


Figure 9. Plots for the odd mode $O_1$ corresponding to figure 8.

where $\kappa^2 = k^2 + m^2$ and $\chi = \kappa^4/\mathcal{G} + \cos\theta + km\mathcal{S}\sin\theta$. Because $\mathcal{S}$ is a function of $y$ this relation can only be viewed as a short-wavelength approximation, suitable when the lengthscale $m^{-1}$ is much shorter than the plate width.

To estimate the neutral stability curves, we look for the smallest value of $\mathcal{G}$ that gives $\omega_i = 0$ over all possible $m$ and $y$. This minimization requires the value of $\mathcal{S}_m(\alpha) = \max_y |\mathcal{S}(y, \alpha)|$, which is plotted in figure 10. Solutions of this algebraic problem are included in figures 5 and 6 for comparison with the numerical data. The
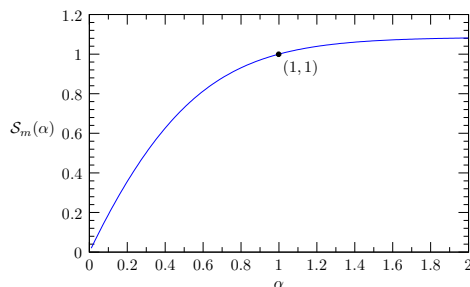
Figure 10. Maximum magnitude of the shear $\mathcal{S}$ over $y$ as a function of $\alpha$.

local approximation gives what appears to be a crude lower bound on the neutral stability curves, and performs best at the lowest and the highest wavenumbers where the eigenfunction possesses short-wavelength structure in $y$ (as demanded by the local theory). For small $k$ and large $\mathcal{G}$, $m \sim k^{-1}$ and the approximate long-wave cut-off is

$$k \approx \frac{4(\cos\theta/3)^{3/4}}{\mathcal{S}_m(\alpha)\sin\theta}\mathcal{G}^{-1/4}.$$

At large $k$, $m \sim k$ and the short-wave cut-off is given by

$$k \approx (3/4)^{3/4} \left[\mathcal{G}\mathcal{S}_m(\alpha)\sin\theta/2\right]^{1/2}.$$

The critical value of $\mathcal{G}$ is poorly predicted by the local analysis because neither $m$ nor $k$ is large there.

The local analysis also predicts that the maximum growth rate occurs for $m = -k\,\mathrm{sign}\,\mathcal{S}$ (*i.e.* wavy perturbations with crests aligned at $45°$ and orientated to take advantage of the destabilizing effect of the local shear), implying a most unstable wavenumber,

$$k \approx \left[\mathcal{G}\mathcal{S}_m(\alpha)\sin\theta/8\right]^{1/2},$$

which is also included in figure 5. Overall, the local analysis offers a useful guide to the stability characteristics, but is only quantitatively accurate at large $k$.

## 5. Qualitative experiments

To provide qualitative verification of the theoretical predictions, we performed a suite of experiments. A 7.6 cm wide, 2.6 cm deep and 1.2 m long channel was mounted on an inclinable table [the achievable fluid flux effectively limited us to an operating range of $(0°, 35°)$]. Thera-Band latex exercise bands were placed on top of the channel to form an elastic skin. Four bands of different thickness were used and were clamped into place using slats. An elongation test indicated that the Young's modulus for all bands was in the range $2 \pm 0.4$ GPa. The sheets used were colour-coded: tan ($2d = 0.12 \pm 0.02$ mm), yellow ($2d = 0.15 \pm 0.02$ mm), red ($2d = 0.20 \pm 0.02$ mm) and green ($2d = 0.25 \pm 0.02$ mm). At the upper end of the channel a reservoir and solid top plate were inserted (the latter to generate the desired base state). Golden syrup ($\rho = 1.4$ g cm$^{-3}$; $\mu = 2.6 \pm 0.2$ and $3.4 \pm 0.2$ Pa s at $20\,°$C) was supplied to the reservoir, and the flux through the duct was controlled
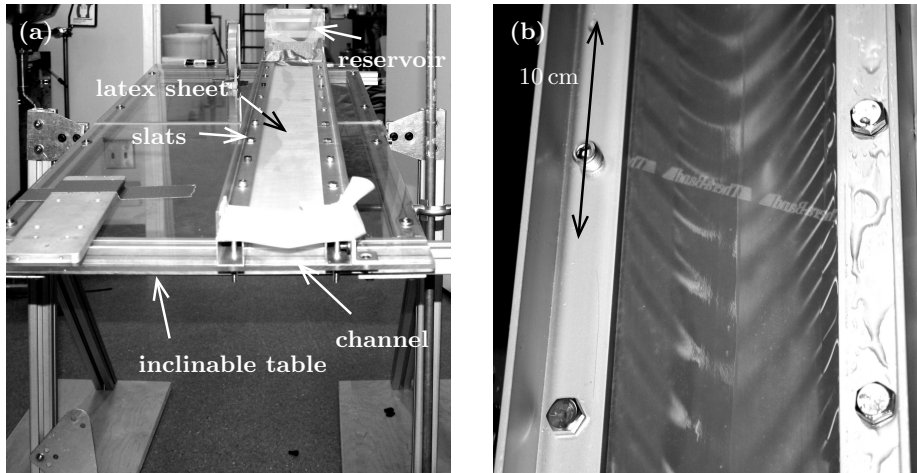
Figure 11. (a) Experimental set-up and (b) mode shape for the yellow sheet at $\theta = 22°$.

manually and made as constant as possible using a valve. For $\theta \lesssim 10°$, experiments could be maintained for several minutes with the help of a pump; for $\theta > 10°$ experiments could be maintained for at least 30 s. Still images of a deflected laser beam at 1/3 s intervals permitted measurements of the wavelength and wavespeed. The experimental set-up is shown in figure 11(a).

With this arrangement, we successfully observed wrinkling of the latex sheet due to the underlying fluid flow: a sample pattern is shown in figure 11(b). Moreover, the wrinkles propagated downstream at speeds that were a small fraction of the average fluid speed. Overall, the observed properties of the wrinkling patterns and the trends on varying the inclination and the thickness of the latex sheet were consistent with the theoretical predictions: for experiments performed at angles below a critical value, the sheet appeared flat; at higher inclination, buckles were observed. As expected from theory, the critical value was order tens of degrees and increased with increasing thickness of the elastic sheet. Similarly, the observed wavelengths were order of centimetres, and decreased with increasing slope and with decreasing thickness of the elastic sheet, whereas the wavespeed increased with slope. Distinct chevron patterns much like the linear eigenfunctions were observed, although the maxima were generally located near the edges, and rarely along the centre-line. Frequently, the maxima on either side were not in phase suggesting a competition between even and odd modes of instability, exactly as in the theory.

Despite this qualitative success, we were unable to provide a quantitative validation of the theory because we found significant problems regarding reproducibility: experiments with apparently identical set-up had variations of as much as $10°$ in onset angle. We believe that the problem originates from some initial compression or tension of the sheet, which is almost impossible to avoid and is unquantifiable. A similar, although less serious, issue arose in our previous experiments with an isolated, sheared elastic sheet (Balmforth *et al.*, 2008). There theory predicted that displacements of the plate in $y$ by fractions of a millimetre could appreciably shift onset. As for that problem, here we anticipate that the presence of tiny amounts of

compression or tension can swamp the shear instability, with compression accentuating it and tension eliminating it.

## 6. Geological application

The surface of "ropy pahoehoe" lava flows has a characteristic corrugated appearance consisting of folds a few centimetres in amplitude and a few centimetres to tens of centimetres in wavelength (Fink & Fletcher, 1978), resulting from some mechanism of compression of the cooled, rheologically distinct upper crust. Based on field studies of solidified flows and movies of active ones, Fink & Fletcher (1978) suggest that wrinkles are formed where a flow encounters a constriction or a sudden change in slope, and the faster moving lava advects upstream crust into crust near the obstacle to compress and buckle it. Beyond the generation point, the flow rotates the wrinkles into their characteristic parabolic shape.

A possible alternative mechanism is suggested by the current study: the corrugations are a manifestation of shear-induced wrinkling. Although our model is a crude approximation of a real lava flow, it does capture the most fundamental features. Particularly regular wrinkles are formed on channelized lava flows bordered by "levees" (Fink & Fletcher, 1978; Garry *et al.*, 2006), providing some justification for our geometry. From a rheological perspective, although lava is a heterogeneous fluid with significant non-Newtonian, temperature-dependent rheology (Griffiths, 2000), a number of observations indicate that our approximation is reasonable at leading order. First, the formation of the upper boundary layer (solid or otherwise) insulates the underlying flow and the temperature in the interior is essentially constant and uniform (Hon *et al.*, 1994). Second, ropes form preferentially relatively close to the vent where the bubble and crystal contents are comparatively low, and so the interior fluid may be approximated as Newtonian. The overlying crust is observed to be a visco-elastic shell, with a brittle upper casing and a high-viscosity lower cushion (Hon *et al.*, 1994). Our elastic plate formulation provides one possible idealization of this crust (*c.f.* Iverson, 1990); we also provide a corresponding analysis for a very viscous fluid plate in Appendix B (*c.f.* Biot, 1961; Fink & Fletcher, 1978). The two models share many common features and we concentrate on the former here. We note that the most immediate short-coming of the model is that it enforces conservation of crust material, whereas stretching and fracture in conjunction with solidification of freshly exposed lava can generate new crust in response to shear.

For the lava flows observed by Fink & Fletcher (1978), $\theta = 5°$, $2y_0 \gtrsim 2.5\,\text{m}$, $2d \lesssim 5\,\text{cm}$ and the wavelength is of order $10\,\text{cm}$. Taking representative values $\alpha = 0.5$ (Calvari *et al.*, 1994), $E = 95\,\text{GPa}$, $\nu = 0.27$ (Schilling *et al.*, 2003) and $\rho = 3000\,\text{kg}\,\text{m}^{-3}$, we predict that a least-stable wavelength of $10\,\text{cm}$ requires a skin thickness of order $0.2\,\text{mm}$. This prediction is appreciably thinner than estimated for the actual flow, but nevertheless is geologically reasonable (Hon *et al.*, 1994). Thus buckling by shear alone is a possible explanation for ropy pahoehoe formation, although the theoretically predicted requirements are at the limits of what is observed. The mode shapes are also in qualitative agreement with the field observations (compare figures 1 and 8).

It is also worth noting that there is a considerable experimental literature on laboratory analogue flows utilizing cooling PEG wax (Griffiths *et al.*, 2003; Garry

*et al.*, 2006, and the references therein). Qualitatively the features produced by these extruded, cooling flows of wax mimic those of real lava flows: they form levees, become channelized and once a solidified skin forms may develop surface texture and regular folding. Our predicted mode shapes are also in qualitative agreement with these laboratory flows.

## 7. Conclusions

In this article we have demonstrated that an elastic plate can be buckled through traction exerted by an underlying fluid shear flow. More precisely, we have explored linear buckling instabilities in an elastic plate clamped over an inclined duct filled with fluid flowing under gravity alone. The varying fluid traction across the top of the duct leads to a destabilizing in-plane shear in the plate, and we have mapped out the conditions under which this effect drives buckling and classified its character. Instability is most readily observed for thin sheets on steep slopes and deep channels, and the most unstable modes take the form of downslope-directed chevron patterns. These patterns resemble the structures seen on the crusts of pahoehoe lava flows, leading us to explore whether crustal shear due to underlying lava flow could be responsible for their formation.

We also successfully conducted a suite of simple experiments to confirm the theory qualitatively. Unfortunately, the experiments were plagued by technical complications. In particular, an uncontrollable amount of slack or tension was probably introduced in the elastic plate when it was initially clamped into place. The resulting lateral compression swamps the shear-induced instability and prevents any quantitative comparison with theory. To surmount this issue, a more sophisticated experiment is needed, which we leave for future work.

Although our main focus has been the buckling of an elastic plate, we have also given a brief discussion of the corresponding problem when the fluid is coated by a thin film of much more viscous fluid. Such a skin can also be buckled by an underlying fluid shear flow, giving another example of G. I. Taylor's analogy between an elastic plate and a viscous sheet. Our formulation of this second problem (containing the fluid equivalents of the Föppl–von Kármán equations) is relatively novel, and we hope that it proves useful in a variety of other physical problems and prompts innovative mathematical analysis.

## Acknowledgements

*Article submitted to Royal Society*

# Appendix A. Derivation of the Föppl–von Kármán equations

This appendix provides an asymptotic derivation of the Föppl–von Kármán equations for the elastic plate from the three-dimensional equilibrium equations. The analysis is essentially identical to that of Ciarlet (1979) (see also Antman, 1995) and we omit details for brevity; novelties are the inclusion of non-dead loads and the discussion of larger displacements.

We return to dimensional variables. The plate is described by Lagrangian coordinates $\hat{\mathbf{X}}$ for the unstressed reference configuration and Eulerian coordinates $\hat{\mathbf{x}} = \hat{\mathbf{X}} + [\hat{\boldsymbol{\xi}}(\hat{\mathbf{X}}), \hat{\zeta}(\hat{\mathbf{X}})]$ for the deformed configuration. The equations are derived in Lagrangian coordinates before being converted into Eulerian.

Conservation of momentum is given by

$$\nabla_{\hat{\mathbf{X}}} \cdot \hat{\mathsf{S}} = \mathbf{0}, \tag{A 1}$$

where subscript $\hat{\mathbf{X}}$ denotes Lagrangian derivatives, $\hat{\mathsf{S}} = \hat{\boldsymbol{\Sigma}}\hat{\mathsf{F}}^\dagger$ is the first Piola–Kirchoff stress tensor, $\hat{\mathsf{F}} = \boldsymbol{\nabla}_{\hat{\mathbf{X}}} \hat{\mathbf{x}}^\dagger$ is the deformation gradient tensor and $\hat{\boldsymbol{\Sigma}}$ is the second Piola–Kirchoff stress tensor. We assume that the material is Hookean, with linear, isotropic constitutive relation

$$\hat{\boldsymbol{\Sigma}} = 2\hat{\mu}\hat{\mathsf{E}} + \hat{\lambda}\operatorname{tr}(\hat{\mathsf{E}})\mathsf{I}, \tag{A 2}$$

where $\hat{\mu}$ and $\hat{\lambda}$ are Lamé constants and $\hat{\mathsf{E}} = (\hat{\mathsf{F}}^\dagger\hat{\mathsf{F}} - \mathsf{I})/2$ is the strain tensor.

Boundary conditions describing fluid forcing of the lower surface and a free upper surface are

$$\hat{\mathsf{S}}^\dagger \cdot \mathcal{N} = \begin{cases} \mathbf{0} & \hat{Z} = d, \\ \hat{\boldsymbol{\tau}}(\hat{\mathbf{x}})\frac{\mathrm{d}s}{\mathrm{d}S} & \hat{Z} = -d, \end{cases} \tag{A 3}$$

where $\mathrm{d}s/\mathrm{d}S = |(\hat{\mathsf{F}}^{-1})^\dagger \cdot \mathcal{N}|$ and $\mathcal{N} = (0,0,1)$ is the normal to the plate in its undeformed configuration.

We pose the following non-dimensionalizations and scalings (emphasizing that the new unhatted variables are distinct from those in the article proper):

$$(\hat{X}, \hat{Y}, \hat{Z}) = (LX, LY, dZ), \quad (\hat{\boldsymbol{\xi}}, \hat{\zeta}) = L'(\delta\boldsymbol{\xi}, \zeta), \quad (\hat{\boldsymbol{\tau}}_h, \hat{\tau}_z) = \hat{\mu}\delta^3(\boldsymbol{\tau}_h, \delta\tau_z), \tag{A 4}$$
$$(\hat{\Sigma}_{XX}, \hat{\Sigma}_{XY}, \hat{\Sigma}_{YY}, \hat{\Sigma}_{XZ}, \hat{\Sigma}_{YZ}, \hat{\Sigma}_{ZZ}) = \hat{\mu}\delta^2(\Sigma_{XX}, \Sigma_{XY}, \Sigma_{YY}, \delta\Sigma_{XZ}, \delta\Sigma_{YZ}, \delta^2\Sigma_{ZZ}),$$

where $\delta = L'/L \ll 1$, $L'$ is a typical out-of-plane displacement and $L$ is a characteristic cross-stream length scale. The scalings for components of $\hat{\boldsymbol{\Sigma}}$ are forced by the governing equations and boundary conditions; we also scale and non-dimensionalize $\hat{\mathsf{S}}$ in the same way. We approximate the equations to leading order in $\delta$, assuming $\Delta = d/L'$ is order unity.

From (A 2) and the scalings for $\hat{\boldsymbol{\Sigma}}$ we find at leading order

$$\boldsymbol{\xi} = -\Delta Z\boldsymbol{\nabla}_H\zeta + \bar{\boldsymbol{\xi}}(X, Y), \quad \partial\zeta/\partial Z = 0, \tag{A 5}$$

where $\bar{\boldsymbol{\xi}}$ is the in-plane displacement of the centre-plane ($Z = 0$) and subscript $H$ denotes components in the $(X, Y)$ plane, and

$$\Sigma_{XX} = \frac{2(\hat{\lambda} + \hat{\mu})}{\hat{\lambda} + 2\hat{\mu}} \left( 2\frac{\partial\xi}{\partial X} + \left[\frac{\partial\zeta}{\partial X}\right]^2 \right) + \frac{\hat{\lambda}}{\hat{\lambda} + 2\hat{\mu}} \left( 2\frac{\partial\eta}{\partial Y} + \left[\frac{\partial\zeta}{\partial Y}\right]^2 \right), \qquad (A\,6)$$

$$\Sigma_{XY} = 2 \left( \frac{\partial\xi}{\partial Y} + \frac{\partial\eta}{\partial X} + \frac{\partial\zeta}{\partial X}\frac{\partial\zeta}{\partial Y} \right), \qquad (A\,7)$$

$$\Sigma_{YY} = \frac{\hat{\lambda}}{\hat{\lambda} + 2\hat{\mu}} \left( 2\frac{\partial\xi}{\partial X} + \left[\frac{\partial\zeta}{\partial X}\right]^2 \right) + \frac{2(\hat{\lambda} + \hat{\mu})}{\hat{\lambda} + 2\hat{\mu}} \left( 2\frac{\partial\eta}{\partial Y} + \left[\frac{\partial\zeta}{\partial Y}\right]^2 \right). \qquad (A\,8)$$

Substituting (A 4) into (A 1) and (A 3) we obtain

$$\frac{\partial\Sigma_{XX}}{\partial X} + \frac{\partial\Sigma_{XY}}{\partial Y} + \frac{1}{\Delta}\frac{\partial\Sigma_{XZ}}{\partial Z} = 0, \qquad (A\,9)$$

$$\frac{\partial\Sigma_{XY}}{\partial X} + \frac{\partial\Sigma_{YY}}{\partial Y} + \frac{1}{\Delta}\frac{\partial\Sigma_{YZ}}{\partial Z} = 0, \qquad (A\,10)$$

$$\frac{\partial S_{XZ}}{\partial X} + \frac{\partial S_{YZ}}{\partial Y} + \frac{1}{\Delta}\frac{\partial S_{ZZ}}{\partial Z} = 0, \qquad (A\,11)$$

subject to

$$(\Sigma_{XZ}, \Sigma_{YZ}) = \begin{cases} \mathbf{0} & Z = 1, \\ \boldsymbol{\tau}_h & Z = -1, \end{cases}, \quad S_{ZZ} = \begin{cases} 0 & Z = 1, \\ \tau_Z & Z = -1, \end{cases} \qquad (A\,12)$$

at leading order. Integrating (A 9)–(A 11) across the thickness of the plate, we obtain the non-dimensional Föppl–von Kármán equations in Lagrangian coordinates as

$$\boldsymbol{\tau}_h = \nabla_H \cdot \mathsf{N}, \quad \frac{8}{3}\Delta^3 \frac{\hat{\lambda} + \hat{\mu}}{\hat{\lambda} + 2\hat{\mu}} \nabla_H^4 \zeta = -\tau_z + \Delta\nabla_H \cdot \boldsymbol{\tau}_h + \nabla_H \cdot (\mathsf{N} \cdot \boldsymbol{\nabla}_H \zeta), \quad (A\,13)$$

where $\mathsf{N} = 4\Delta\mathsf{e} + 4\Delta\hat{\lambda}\,\mathrm{tr}(\mathsf{e})\mathsf{I}_H/(\hat{\lambda} + 2\hat{\mu})$ and $2\mathsf{e} = \boldsymbol{\nabla}_H\bar{\boldsymbol{\xi}} + \boldsymbol{\nabla}_H\bar{\boldsymbol{\xi}}^\dagger + \boldsymbol{\nabla}_H\zeta\boldsymbol{\nabla}_H\zeta$. The term $\Delta\nabla_H \cdot \boldsymbol{\tau}_h$ in (A 13) can be omitted on the grounds that if the pressure perturbation scales as $\hat{\mu}\delta^4$, then the in-plane traction perturbations also scale as $\hat{\mu}\delta^4$ but our choice in (A 4) is one order lower (to accommodate larger in-plane tractions in the base state, but for which $\Delta\nabla_H \cdot \boldsymbol{\tau}_h = 0$).

Finally, we convert to Eulerian coordinates by noting that $\nabla_H = \nabla_h + \mathcal{O}(\delta^2)$ and the leading order equations remain valid. The system (A 13) is now equivalent to the system (2.3) on redimensionalizing and identifying $\nu = \hat{\lambda}/2(\hat{\lambda} + \hat{\mu})$ and $E = \hat{\mu}(3\hat{\lambda} + \hat{\mu})/(\hat{\lambda} + \hat{\mu})$.

The terms in (A 13) all remain at the same leading order provided $\delta^{1/3} \ll \Delta \ll \delta^{-1/3}$, which limits the magnitude of $\Delta$. In turn, this limits how large we may take $\mathcal{G}$ to become in order for the plate equations to remain valid. Specifically, we find $\mathcal{G} \ll y_0/d$, which allows for relatively large numerical values of $\mathcal{G}$ provided the plate is thin enough.

## Appendix B. A viscous fluid plate

In this appendix, we present complementary results for the buckling of a thin, very viscous fluid overlying the channel. Such skins have similar behaviour in compression

to elastic beams (*c.f.* the beam analogy of Ribe, 2004) and we find a similar shear instability to that explored in the main text.

We derive the fluid equivalent of the Föppl–von Kármán equations; the approach is similar to that given in Appendix A except we remain in Eulerian coordinates. We commence with a dimensional formulation. The skin is initially uniform, flat and is contained between $\alpha y_0 - d \leq \hat{z} \leq \alpha y_0 + d$. At later times it is contained between $\hat{h}^-(\hat{x}, \hat{y}, \hat{t}) \leq \hat{z} \leq \hat{h}^+(\hat{x}, \hat{y}, \hat{t})$.

Conservation of momentum (ignoring gravity) and mass in the three-dimensional skin are given by

$$\hat{\boldsymbol{\nabla}} \cdot \hat{\boldsymbol{\sigma}}_p = \mathbf{0}, \quad \hat{\nabla} \cdot \hat{\mathbf{u}}_p = 0, \quad \hat{\boldsymbol{\sigma}}_p = -\hat{p}_p \mathsf{I} + \mu_p \left( \hat{\boldsymbol{\nabla}} \hat{\mathbf{u}}_p + \hat{\boldsymbol{\nabla}} \hat{\mathbf{u}}_p^\dagger \right), \qquad \text{(B\,1)}$$

where subscript $p$ denotes quantities pertaining to the plate fluid. Boundary conditions are

$$\hat{\boldsymbol{\sigma}}_p \cdot \hat{\mathbf{n}} = \begin{cases} \mathbf{0} & \hat{z} = \hat{h}^+ \\ \hat{\boldsymbol{\tau}} & \hat{z} = \hat{h}^- \end{cases}, \quad \hat{\mathbf{u}}_p = \hat{\mathbf{u}} \quad \text{on } \hat{z} = \hat{h}^-,$$

$$\frac{\partial \hat{h}^\pm}{\partial \hat{t}} + \hat{u}_p \frac{\partial \hat{h}^\pm}{\partial \hat{x}} + \hat{v}_p \frac{\partial \hat{h}^\pm}{\partial \hat{y}} = \hat{w}_p \quad \text{on } \hat{z} = \hat{h}^\pm. \qquad \text{(B\,2)}$$

We non-dimensionalize and scale these equations similarly to (A\,4):

$$(\hat{x}, \hat{y}, \hat{z} - \alpha y_0, \hat{h}^\pm) = (Lx, Ly, dz, dh^\pm), \quad \hat{p}_p = \mu_p \frac{U}{L} \epsilon^2 p_p,$$

$$\hat{\mathbf{u}}_p = U \epsilon(\epsilon u_p, \epsilon v_p, w_p), \quad (\hat{\boldsymbol{\tau}}_h, \hat{\tau}_z) = \mu_p \frac{U}{L} \epsilon^3 (\boldsymbol{\tau}_h, \epsilon \tau_z), \qquad \text{(B\,3)}$$

$$(\hat{\sigma}_{pxx}, \hat{\sigma}_{pxy}, \hat{\sigma}_{pyy}, \hat{\sigma}_{pxz}, \hat{\sigma}_{pyz}, \hat{\sigma}_{pzz}) = \mu_p \frac{U}{L} \epsilon^2 (\sigma_{pxx}, \sigma_{pxy}, \sigma_{pyy}, \epsilon \sigma_{pxz}, \epsilon \sigma_{pyz}, \epsilon^2 \sigma_{pzz}),$$

where $L$ is the length-scale of horizontal variation, $\epsilon = d/L \ll 1$ and the velocity scale $U$ is assumed order unity, which must be verified *a posteriori*. We approximate the equations to leading order in $\epsilon$.

From (B\,1) and the scalings of $\hat{\boldsymbol{\sigma}}_p$ we find to leading order

$$u_p = -z \frac{\partial w_p}{\partial x} + \bar{u}_p(x, y), \quad v_p = -z \frac{\partial w_p}{\partial y} + \bar{v}_p(x, y), \quad \frac{\partial w_p}{\partial z} = 0, \qquad \text{(B\,4)}$$

and

$$\sigma_{pxx} = 4 \frac{\partial u_p}{\partial x} + 2 \frac{\partial v_p}{\partial y}, \quad \sigma_{pxy} = \frac{\partial u_p}{\partial y} + \frac{\partial v_p}{\partial x}, \quad \sigma_{pyy} = 2 \frac{\partial u_p}{\partial x} + 4 \frac{\partial v_p}{\partial y}, \qquad \text{(B\,5)}$$

where the barred velocities are the analogues of the centre-plane displacement for the elastic plate. The governing equations become

$$\frac{\partial \sigma_{pjx}}{\partial x} + \frac{\partial \sigma_{pjy}}{\partial y} + \frac{\partial \sigma_{pjz}}{\partial z} = 0, \qquad \text{(B\,6)}$$

subject to

$$\sigma_{pjz} - \frac{\partial h^\pm}{\partial x} \sigma_{pjx} - \frac{\partial h^\pm}{\partial y} \sigma_{pjy} = \begin{cases} 0 & z = h^+, \\ \tau_j & z = h^-, \end{cases} \qquad \text{(B\,7)}$$
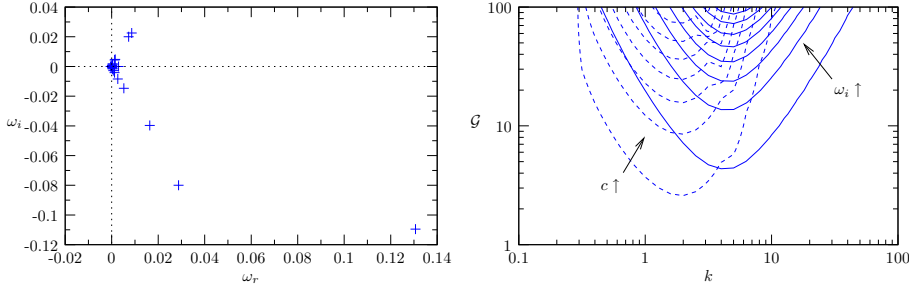
Figure 12. The fluid plate. (a) The spectrum of $\omega$ for $\mathcal{G} = 50$, $\alpha = \tan\theta = 1$ and $k = 1$. Modes are converged except very close to the origin. (b) The growth rate (solid contours at intervals of 0.02 from 0.01) and wavespeed (dashed contours at intervals of 0.002 from 0.001) of the most unstable mode in $(k, \mathcal{G})$-space for $\alpha = \tan\theta = 1$.

where $j$ denotes $x$, $y$ or $z$. The kinematic conditions imply

$$\frac{\partial h^+}{\partial t} = \frac{\partial h^-}{\partial t} = w_p(x, y, t), \tag{B 8}$$

and we have $h^+ - h^- = 2$ at leading order. We define $2h = h^+ + h^-$.

Now integrating (B 6) across the plate and imposing (B 7), we obtain the fluid equivalents of the Föppl–von Kármán equations

$$\boldsymbol{\tau}_h = \nabla_h \cdot \mathsf{N}, \quad \frac{8}{3}\nabla_h^4 w_p = -\tau_z + \nabla_h \cdot \boldsymbol{\tau}_h + \nabla_h \cdot (\mathsf{N} \cdot \boldsymbol{\nabla}_h h), \tag{B 9}$$

where $\mathsf{N} = 4[\mathsf{e} + \mathrm{tr}(\mathsf{e})\mathsf{I}_h]$ with $2\mathsf{e} = \boldsymbol{\nabla}_h(\bar{u}_p, \bar{v}_p) + \boldsymbol{\nabla}_h(\bar{u}_p, \bar{v}_p)^\dagger - 2h\boldsymbol{\nabla}_h\boldsymbol{\nabla}_h w_p$. As for the elastic case, we neglect $\nabla_h \cdot \boldsymbol{\tau}_h$.

Re-dimensionalizing we obtain the governing equations

$$\hat{\boldsymbol{\tau}}_h = \nabla_h \cdot \hat{\mathsf{N}}, \quad \frac{8}{3}\mu_p d^3 \nabla_h^4 \hat{w}_p = -\hat{\tau}_z + \nabla_h \cdot \left(\hat{\mathsf{N}} \cdot \boldsymbol{\nabla}_h \hat{h}\right), \tag{B 10}$$

where $\hat{\mathsf{N}} = 4\mu_p d[\hat{\mathsf{e}} + \mathrm{tr}(\hat{\mathsf{e}})\mathsf{I}_h]$ and $2\hat{\mathsf{e}} = \hat{\boldsymbol{\nabla}}_h(\hat{\bar{u}}_p, \hat{\bar{v}}_p) + \hat{\boldsymbol{\nabla}}_h(\hat{\bar{u}}_p, \hat{\bar{v}}_p)^\dagger - 2h\hat{\boldsymbol{\nabla}}\hat{\boldsymbol{\nabla}}_h \hat{w}_p$. At the side-walls, $\hat{y} = \pm y_0$, we have the equivalent of the clamped boundary conditions, $\hat{\bar{u}}_p = \hat{\bar{v}}_p = \hat{w}_p = \partial\hat{w}/\partial\hat{y} = 0$. The kinematic conditions and continuity of velocity imply $\partial\hat{h}/\partial\hat{t} = \hat{w}_p = \hat{w}$ and $\hat{u}_p = \hat{v}_p = 0$ on the base of the plate.

Using (B 10) and the associated boundary conditions in place of (2.3) in the governing equations (2.1)–(2.7), we obtain the equivalent system for a viscous plate (identifying $\zeta$ with $h$). On non-dimensionalizing according to (2.8) with $\hat{\bar{\mathbf{u}}} = \bar{\mathbf{u}}\rho g y_0^3/\mu_p d$, we arrive at essentially identical stability equations to (4.1)–(4.8) except that the biharmonic operator acts on $w$ rather than $\zeta$ and

$$\mathcal{G} = \frac{3\mu y_0^3}{8\mu_p d^3}.$$

We note that

for the viscous plate equation (B 10) to be valid, the base state velocity within the plate must scale according to (B 3) and so $\mu_p d^3 \lesssim \rho g y_0^5$.

Sample stability results for this model are shown in figure 12. Panel (a) plots the eigenvalue spectrum for a particular set of parameter values. The two distinctly unstable modes have a similar perturbation profile to those plotted in figures 8 and 9 with even and odd chevrons directed downslope. The origin of the complex plane forms a limit point of the spectrum; for modes closer and closer to it, more and more cross-slope oscillations are accommodated. The dispersion relation for the most unstable mode is plotted in panel (b). As for the elastic case, a window of intermediate wavelengths are unstable.

# References

ANTMAN, S. S. 1995 *Nonlinear problems of elasticity*. New York: Springer.

BALMFORTH, N. J., CRASTER, R. V. & SLIM, A. C. 2008 On the buckling of elastic plates. *Q. J. Mech. Appl. Math.* doi:10.1093/qjmam/hbn002.

BIOT, M. 1961 Theory of folding of stratified viscoelastic media and its implications in tectonics and orogenesis. *Bull. Geol. Soc. Amer.* **72** (11), 1595–1620.

CALVARI, S., COLTELLI, M., NERI, M., POMPILIO, M. & SCRIBANO, V. 1994 The 1991–1993 Etna eruption: chronology and lava flow-field evolution. *Acta Vulcanol.* **4**, 1–14.

CIARLET, P. G. 1979 Une justification des équations de von Kármán. *C. R. Acad. Sc. Paris Série A* **288**, 469–472.

FINK, J. H. & FLETCHER, R. C. 1978 Ropy pahoehoe: surface folding of a viscous liquid. *J. Volcanol. Geoth. Res.* **4**, 151–170.

GARRY, W. B., GREGG, T. K. P., SOULE, S. A. & FORNARI, D. J. 2006 Formation of submarine lava channel textures: Insights from laboratory simulations. *J. Geophys. Res.* **111**, B03104.

GRIFFITHS, R. W. 2000 The dynamics of lava flows. *Annu. Rev. Fluid Mech.* **32** (1), 477–518.

GRIFFITHS, R. W., KERR, R. & CASHMAN, K. 2003 Patterns of solidification in channel flows with surface cooling. *J. Fluid Mech.* **496**, 33–62.

HON, K., KAUAHIKAUA, J., DENLINGER, R. & MACKAY, K. 1994 Emplacement and inflation of pahoehoe sheet flows: observations and measurements of active lava flows on Kilauea Volcano, Hawaii. *Geol. Soc. Am. Bull.* **106**, 351–370.

HUANG, R. & SUO, Z. 2002 Wrinkling of a compressed elastic film on a viscous layer. *J. Appl. Phys.* **91** (3), 1135–1142.

IVERSON, R. M. 1990 Lava domes modelled as brittle shells that enclose pressurized magma, with application to Mount St. Helens. In *Lava flows and domes: emplacement mechanisms and hazard implications* (ed. J. H. Fink), *IAVCEI Proc. Volcanol.*, vol. 2, pp. 47–69. IUGG Congress, Vancouver, BC, Berlin: Springer.

LOVE, A. 1944 *A treatise on the mathematical theory of elasticity*. Dover.

Luo, H. & Pozrikidis, C. 2006 Buckling of a flush-mounted plate in simple shear flow. *Arch. Appl. Mech.* **76** (9), 549–566.

Luo, H. & Pozrikidis, C. 2007 Buckling of a pre-compressed or pre-stretched membrane in shear flow. *Intl. J. Solids Struc.* **44** (24), 8074–8085.

Mansfield, E. H. 1964 *The bending and stretching of plates*. Oxford: Pergamon, international series of monographs on aeronautics and astronautics.

Ribe, N. M. 2004 Coiling of viscous jets. *Proc. R. Soc. Lond.* A **460**, 3223–3239.

Rosenhead, L. 1963 *Laminar boundary layers*. Clarendon Press.

Schilling, F. R., Sinogeikin, S. V., Hauser, M. & Bass, J. D. 2003 Elastic properties of model basaltic melt compositions at high temperatures. *J. Geophys. Res.* **108**, 2304.

Trefethen, L. 2000 *Spectral methods in MATLAB*. SIAM.

Weideman, J. A. C. & Reddy, S. C. 2000 A MATLAB differentiation matrix suite. *ACM Transactions on Mathematical Software* **26** (4), 465–519.

Wong, Y. W. & Pellegrino, S. 2006 Wrinkled membranes. Part I: experiments. *J. Mech. Materials Struct.* **1**, 3–25.